

COMPREHENSIVE MODELLING OF THE EARTH'S MAGNETIC FIELD: CURRENT STATUS AND FUTURE PROSPECTS

Terence J. Sabaka¹ and Nils Olsen²

¹Geophysics Branch, Code 921, NASA Goddard Space Flight Center, Greenbelt, MD 20771
(sabaka@geomag.gsfc.nasa.gov).

²Danish Space Research Institute, Juliane Maries Vej 30, DK - 2100 Copenhagen Ø, Denmark

ABSTRACT

To date, the best model derived using a comprehensive approach has been based upon data from the POGO and Magsat satellites as well as ground-based observatories and spanned 1960-1985. This paper presents an extension to that model which analyzes scalar data from the CHAMP satellite and vector and scalar data from the Ørsted satellite and is valid through mid-2002. In order to more properly describe toroidal fields in the satellite sampling shells, the associated F -regions currents are treated as lying in meridional planes which conform to the contours of the ambient field. Furthermore, for the Ørsted sampling shell, these currents are treated as diurnally continuous. In addition to the obvious extension of the main field secular variation, the new model exhibits a superior lithospheric field with far less noise content than the previous best model, and the F -regions currents agree well with previous Magsat results while a weaker meridional current system associated with the equatorial electrojet is inferred from Ørsted data. Several future objectives have been enumerated and several may be attainable in the short term.

1. INTRODUCTION

Within a few thousand kilometers of Earth's surface the magnetic field is rich in measurable contributions from several distinct current systems. However, the spatial and temporal scales of some of these constituent fields overlap, making it difficult to separate their effects from samplings of the observed field. A very successful approach known as "comprehensive modelling" has been developed to overcome this problem (see Langel et al., 1996; Sabaka et al., 2002). It entails the parameterization and co-estimation of fields associated with the major current sources in the near-Earth regime from field measurements taken from permanent ground-based observatories and satellite mapping missions, taking into account the crucial covariance between these

fields. The result is a more proper partitioning of the amalgamated signal amongst the physical sources in a weighted least-squares sense. These parameterized fields include those of core and lithospheric origin, magnetospheric and ionospheric origin along with associated induced contributions, and toroidal magnetic fields produced by insitu poloidal currents that impinge the thin sampling shells of the satellites. Surface and satellite data together facilitate separation via their relative radial orientations with respect to the sources and their spatial and temporal sampling extents. Note that describing the complexities of the geomagnetic field is quite challenging even during magnetically quiet periods, and so these studies have been restricted to those periods where roughly $K_p \leq 2^0$.

The most successful published comprehensive model (CM) is CM3 (Sabaka et al., 2002), which spanned 1960-1985 and was derived from observatory data as well as data from the POGO and Magsat satellite missions. However, while the POGO data covered years 1965-1971, the data were only scalar intensity, and while Magsat delivered accurate vector data, it only sampled a six month period from November 1979 to May 1980 at only two local times, dawn and dusk. Hence, global data coverage is severely limited in CM3. Finally, after a roughly twenty year hiatus, the Danish Ørsted satellite was launched in February of 1999 and in July of 2000 the German CHAMP satellite was launched, both high-precision scalar and vector magnetic mapping missions. Both satellites are in near-polar orbits and have already provided several years of quality data over all local times. Clearly, a CM augmented with these data will come much closer to its objective of properly representing the quiet-time, near-Earth magnetic field.

The remainder of this paper reports on a natural extension of CM3, denoted CM4, in which scalar data from CHAMP and vector and scalar data from Ørsted have been incorporated, along with all available observatory data through 2000. Slight modifications have been made to the CM3 parameterization in order to accommodate these data and include 1) an extension of the main field secular vari-

ation (SV) basis functions through 2010; 2) insitu quasi-dipole (QD) meridional poloidal currents in the Magsat sampling shell; and 3) insitu QD meridional poloidal currents in the Ørsted sampling shell which are continuous in diurnal time. A comparison of CM3 and CM4 will be given and the above modifications will be further explained. However, a detailed description of these models is beyond the scope of this paper, but the interested reader is referred to Sabaka et al. (2002). In addition, future directions will be outlined.

2. DATA SELECTION

2.1. Observatory Data

As CM4 is an extension of CM3, much of the data is common to both. CM3 incorporated observatory hourly means (OHMs) for the quietest day of the month, as determined by K_p , at two sampling rates: 1) the OHM values closest to 0100 local time for the entire 1960-1985 span of the model, denoted as OHM_1AM, and 2) OHMs every two hours on those quiet days during the POGO and Magsat missions envelopes, denoted as OHM_MUL. This former rate allows for the determination of broad-scale main field SV, whilst the latter rate is sufficient for analyzing up to a 6 h diurnal period. For CM4, the OHM values closest to 0100 local time on the quietest day per month were extended through 2000. The spatial and temporal distribution of these data are shown in Fig. 1. Post 1985 temporal distributions are consistent with earlier epochs with a conspicuous rise in reporting stations post 1995. In addition, station breaks (Langel et al., 1982) were introduced at times where baseline jumps have occurred. This leads to a total of 340 OHM_1AM and 216 OHM_MUL stations considered in this model.

2.2. Satellite Data

Of the four satellite data sets used, the POGO and Magsat scalar data sets are identical to those used in CM3 and are described in Sabaka et al. (2002). The Magsat vector data, however, have been reselected for CM4 (Purucker, 2000) in order to achieve denser coverage for improved lithospheric field modelling. They have been selected for sub 20 arcsec accuracy per attitude flags during quiet conditions in which $K_p \leq 1^0$ for the time of observation and $K_p \leq 2^0$ for the previous 3 h interval. The data have been decimated from the original 16 Hz to 0.02 Hz. Ørsted and CHAMP data were selected for quiet conditions where $K_p \leq 1^+$ for the time of observation and $K_p \leq 2^0$ for the previous 3 h interval. In addition, the D_{st} index was required to be within ± 20 nT. The Ørsted data span March 1999 to July 2002 while the CHAMP data span August 2000 to July 2002. During this period both satellite orbits precessed through all local times. A comparison of

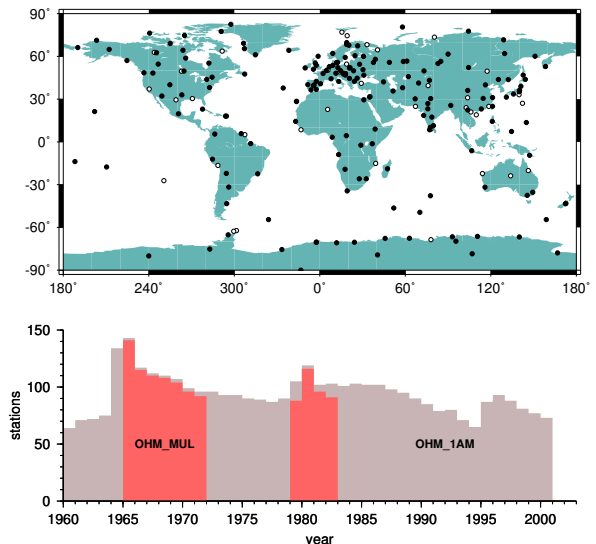


Figure 1. Spatial and temporal distributions of observatory data. The top panel shows observatory locations where only 0100 local time hourly means are used (open circles) or both 0100 and multiple hourly means are used (black circles). The bottom panel shows a histogram of the number of stations contributing either 0100 (OHM_1AM) or multiple hourly (OHM_MUL) means to the particular 1 y bin.

the local time distribution for satellite data is shown in Fig. 2, separately for scalar and vector data. The Ørsted dawn and dusk distribution is weak, but is complemented by Magsat data. Vector and scalar data were used at all latitudes at a sampling rate of 1 Hz. All satellite data were weighted proportional to $\sin \theta$ to simulate an equal-area distribution.

3. MODIFIED PARAMETERIZATION

The parameterization of field sources in CM4 closely follows that of CM3. The core and lithospheric fields are together expressed as the negative gradient of a potential function represented by a degree and order 65 internal spherical harmonic (SH) expansion in geographic coordinates, with SV represented by cubic B-splines through degree and order 13 (see Sabaka et al., 1997). The knot spacing was kept at 2.5 y and merely extended to 2010. Thus, for $n \leq 13$ each gauss coefficient is parameterized by 24 coefficients. Because OHMs are field rather than derivative measurements, and because of their close proximity to lithospheric sources, a set of static vector biases is solved for at each station, including its breaks. These biases represent presumably small-scale lithospheric anomalies whose wavelengths are above the SH truncation level. Though CM4 attempts to model the major quiet time signature of the field, baselines can still be different in the OHM_1AM versus OHM_MUL data, and so separate sets of biases are determined for each.

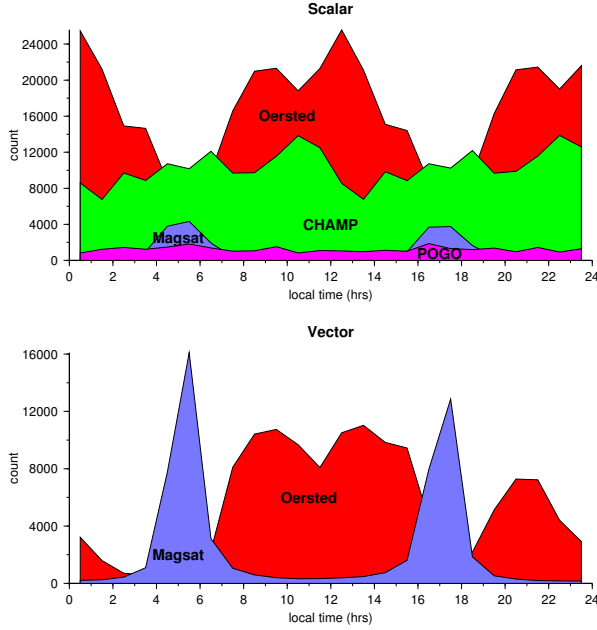


Figure 2. Local time distribution of scalar (top) and vector (bottom) satellite data.

The currents responsible for the ionospheric field are considered to flow in a thin spherical shell at about $h = 110$ km altitude. Hence, the field is expressed as the negative gradient of a potential function at surface and satellites altitudes, constrained to have radial continuity across the current sheet. The ionospheric parameterization employs harmonic functions endowed with symmetry provided by a quasi-dipole coordinate system (Richmond, 1995), which is aligned with the ambient magnetic field. Temporally, these functions are mainly sun-synchronous, but slightly slower and faster modes are also present with a maximum period of 6 h, and are modulated with annual and semi-annual seasonal variability. Spatially, they have high QD latitudinal resolution in order to model the equatorial electrojet (EEJ). Induced contributions are accounted for by using an *a priori* four layer, 1-D, radially varying conductivity model derived from Sq and D_{st} data at selected European observatories (Olsen, 1998). Solar activity influence is introduced through an amplification factor, assumed to be equal for all functions, which is a function of a 3-monthly moving mean of absolute $F_{10.7}$ solar radio flux values (Olsen, 1993). This means that increasing solar flux inflates the whole ionospheric and associated induced current system without changing its shape.

The major sources of the magnetospheric field are currents which flow in the magnetotail, magnetopause, and ring-current complexes. Hence, the field is cast as the negative gradient of a potential function represented by an external SH expansion in dipole coordinates, which has regular daily and seasonal periodicities. Ring current variability is mod-

elled as a linear function of the D_{st} index for external dipole terms only. Because of a lag in availability of the final index, provisional D_{st} has been used for data during and after 2001. The induced contributions of the magnetosphere are treated in a similar manner as the ionosphere and are thus coupled with an internal SH expansion via the same *a priori* conductivity model.

3.1. F -region Currents

Magsat and Ørsted sample the magnetic field in thin shells bounded roughly between 400 to 750 km altitude. Consequently, these measurements contain contributions from toroidal magnetic fields due to poloidal F -region currents \mathbf{J} , which couple the ionosphere and magnetosphere. Hence, this field is not curl-free and cannot be expressed as the gradient of a potential. In CM3, which analyzed Magsat vector data only, these coupling currents were assumed to be purely radial and were only sampled at two local times. However, Olsen (1997a) found evidence of a strong J_θ component in Magsat, and so for CM4 \mathbf{J} is considered QD meridional. Because the coupling current morphology is also highly influenced by the ambient magnetic field, QD symmetric functions are again used here. Since Ørsted samples all local times, a continuous diurnal representation may now be attempted for toroidal \mathbf{B} , at least in the Ørsted shell. Radial continuity between the Magsat and Ørsted shells will be deferred for future work, and so separate parameterizations are used for Magsat dawn and dusk and Ørsted.

Following Backus (1986), Olsen (1997a) showed that toroidal \mathbf{B} and associated poloidal \mathbf{J} may be expressed in spherical coordinates (r, θ, ϕ) as

$$\mathbf{B} = \begin{pmatrix} 0 \\ \frac{1}{\sin \theta} \frac{\partial}{\partial \phi} \Phi \\ -\frac{\partial}{\partial \theta} \Phi \end{pmatrix}, \quad (1)$$

$$\mathbf{J} = \begin{pmatrix} -\Delta_s(r\Phi) \\ \frac{1}{r} \frac{\partial}{\partial \theta} (r\Phi)' \\ \frac{1}{r \sin \theta} \frac{\partial}{\partial \phi} (r\Phi)' \end{pmatrix} \frac{1}{\mu_0}, \quad (2)$$

where Δ_s is the angular part of the Laplacian, the prime indicates differentiation in r , and Φ is the toroidal scalar function

$$\Phi(t, \mathbf{r}) = \Re \left\{ \sum_{n,m,s,p} \phi_{nsp}^m(r) T_{nsp}^m(t, \theta_q, \phi_q) \right\}, \quad (3)$$

with

$$T_{nsp}^m(t, \theta_q, \phi_q) = Y_n^m(\theta_q, \phi_q) \times \exp i s \phi_s(t) \times \exp i p \phi_p(t_{mut}(t)). \quad (4)$$

$Y_n^m(\theta_q, \phi_q)$ is the usual Schmidt quasi-normalized surface spherical harmonic function of degree n and order m evaluated at QD coordinates

$(\theta_q(\theta, \phi), \phi_q(\theta, \phi))$, but these may be expanded in terms of $Y_l^k(\theta, \phi)$ via spherical transforms. Thus, T_{nsp}^m is QD symmetric on a particular reference sphere and is simply a linear combination of the Y_l^k over k and l , modulated by periodic time functions in QD longitude ϕ_q . The arguments of these time functions include s and p , which are the seasonal and diurnal integer wave numbers, respectively, the seasonal time angle ϕ_s , which has a period of 1 y and is a function of UT t , and the diurnal time angle ϕ_p , which has a period of 24 h and is a function of magnetic universal time (MUT) t_{mut} . The MUT of an observer is closely related to the observer's magnetic local time (MLT) t_{mlt} defined as

$$t_{mlt}(t) = (180^\circ + \phi_{d,o} - \phi_{d,s}(t))/15, \quad (5)$$

where if the dipole longitude of the observer, $\phi_{d,o}$, and the sub-solar point, $\phi_{d,s}(t)$, are in degrees, then $t_{mlt}(t)$ is in hours. Thus, MUT is simply the MLT at the dipole prime meridian ($\phi_{d,o} = 0^\circ$), which runs roughly through central S. America.

In CM3, the radial dependence of Φ was chosen to be $1/r$ which from eq. 2 leads to $J_\theta = J_\phi = 0$. To obtain QD meridional \mathbf{J} , one selects from two classes of admissible Φ : 1) those with a radial dependence of $1/r$, and 2) those which are QD zonal, i.e., $m = 0$. Clearly, only this second class will contribute to the horizontal portion of the currents $\mathbf{J}_h = (J_\theta, J_\phi)^T$. To show that \mathbf{J}_h lies in QD meridional planes, let $f(t, r, \theta_q) = (r\Phi(t, r, \theta_q))'$, but from eq. 2

$$\mathbf{J}_h = \frac{1}{\mu_0} \nabla_h f(t, r, \theta_q), \quad (6)$$

$$= \frac{1}{\mu_0} \frac{\partial f}{\partial \theta_q} \nabla_h \theta_q, \quad (7)$$

where ∇_h is the surface gradient. Therefore, \mathbf{J}_h is a multiple of $\nabla_h \theta_q$ and thus lies in QD meridional planes. Let this component be denoted as J_{θ_q} . The radial dependence of these functions is obtained by following Backus (1986) and Olsen (1997a) who consider a Taylor series expansion of ϕ_{nsp}^m around the shell mean radius, b , such that

$$\phi_{nsp}^m(r) = \left(\frac{R}{r}\right) \sum_j \phi_{nspj}^m \frac{\rho^j}{j!}, \quad (8)$$

where $\rho = (r - b)/R$ and R is the reference radius. Only the $j = 0, 1$ terms are retained for the QD zonal terms in the Magsat and Ørsted models, and only the $j = 1$ terms contribute to \mathbf{J}_h . Thus, the Φ parameterizations used for Magsat dawn and dusk are

$$\Phi(t, \mathbf{r}) = \Re \left\{ \sum_{s=0}^2 \sum_{n=1}^{40} \sum_{m=0}^{\min(n,4)} \phi_{ns00}^m T_{ns0}^m(t, \theta, \phi) + \sum_{s=0}^2 \sum_{n=1}^{40} \rho \phi_{ns01}^0 T_{ns0}^0(t, \theta, \phi) \right\} \left(\frac{R}{r}\right), \quad (9)$$

where $b = 6801.2$ km for dawn and $b = 6786.2$ km for dusk and $R = 6371.2$ km for both. As with CM3,

Table 1. Number of parameters in each field source.

Field source	Number of parameters
Observatory biases	1,668
Core/lithosphere	8,840
Ionosphere	5,520
Magnetosphere	800
Magsat coupling currents	2,328
Ørsted coupling currents	6,120
Total	25,276

the seasonal phase angle is fixed due to the limited seasonal coverage of Magsat. This results in retaining only terms in $\cos s\phi_s(t)$, giving a total of 1164 coefficients in each expansion. For Ørsted

$$\Phi(t, \mathbf{r}) = \Re \left\{ \sum_{s=-2}^2 \sum_{p=0}^4 \sum_{m=p-1}^{p+1} \sum_{n=\max(1, |n|)}^{|n|+40} \phi_{nsp0}^m T_{nsp}^m(t, \theta, \phi) + \sum_{s=-2}^2 \sum_{p=0}^4 \sum_{n=1}^{40} \rho \phi_{nsp1}^0 T_{nsp}^0(t, \theta, \phi) \right\} \left(\frac{R}{r}\right), \quad (10)$$

where $b = 7121.2$ km and $R = 6371.2$ km. The total number of coefficients in the expansion is 6120. These ranges on s , p , n , and m were chosen to match those of the ionosphere, which it couples, since Ørsted vector data give full local time coverage. Because the bulk of toroidal \mathbf{B} is usually perpendicular to the ambient magnetic field, it is assumed that scalar measurements will not be sensitive to it. Thus, only Magsat and Ørsted vector measurements are considered functions of the ϕ_{nspj}^m .

4. ESTIMATION PROCEDURE

4.1. Iteratively Reweighted Least-Squares

Let \mathbf{x} be the vector of model parameters collected from each field source and let $\mathbf{a}(\mathbf{x})$ be the model prediction corresponding to the vector of observed field measurements, \mathbf{d} . For CM4, $\dim \mathbf{x} = 25,276$ and $\dim \mathbf{d} = 1,762,677$. The number of parameters in each source is given in Table 1. Clearly, the estimation of \mathbf{x} from \mathbf{d} is an over-determined inverse problem. If the model residuals, $\mathbf{e} = \mathbf{d} - \mathbf{a}(\mathbf{x})$, are Gaussian distributed, then a weighted least-squares estimate, which minimizes the ℓ_2 norm of a vector, would provide the maximum-likelihood estimate. However, this is surely not the case due to data and theory errors (Walker & Jackson, 2000). Hence, the iteratively reweighted least-squares (IRLS) approach is employed here (see Huber, 1964; Constable, 1988). It is a hybrid method whose cost function contains two terms: $\|\mathbf{e}_G\|_2$ and $\|\mathbf{e}_L\|_1$, where \mathbf{e}_G and \mathbf{e}_L are the subvectors of \mathbf{e} whose distributions are considered Gaussian and Laplacian, respectively. Hence,

large residuals will be treated as Laplacian and will not unduly influence the parameter estimate. Operationally, IRLS may be cast in the framework of the usual least-squares method by employing a special data weight (inverse covariance) matrix, \mathbf{W} , which varies at each iteration in response to changes in \mathbf{e}_G and \mathbf{e}_L . This matrix reflects a Huber distribution, which has a Gaussian core ($\sigma < 1.5$) and Laplacian tails, where σ is the standard deviation. Assuming uncorrelated errors (a diagonal \mathbf{W}), IRLS assigns Huber weights to the k -th data point at the n -th iteration as a function of its standard deviation σ_k and current residual value $e_{k,n}$ as

$$w_{k,n} = \frac{1}{\sigma_k^2} \min \left(\frac{c\sigma_k}{|e_{k,n}|}, 1 \right), \quad (11)$$

with $c = 1.5$. The $w_{k,n}$ for satellite data are multiplied by $\sin \theta$ as stated earlier. In this study, *a priori* information is to be injected for purposes of physical plausibility and regularization and takes the form of k additional quadratic terms in the cost function. Formally, these ℓ_2 norms describe \mathbf{x} as the realization of k Gaussian processes having covariances of $(\lambda_i \Lambda_i)^{-1}$, $i = 1, \dots, k$. Thus, the damping parameters, λ_i , and Λ_i remain static throughout IRLS and are exempt from modifications as in eq. 11.

The non-linear IRLS cost function

$$\begin{aligned} \mathcal{L}(\mathbf{x}) = & (\mathbf{d} - \mathbf{a}(\mathbf{x}))^T \mathbf{W} (\mathbf{d} - \mathbf{a}(\mathbf{x})) + \\ & \sum_{i=1}^k \lambda_i \mathbf{x}^T \Lambda_i \mathbf{x}, \end{aligned} \quad (12)$$

is minimized to obtain an estimate of \mathbf{x} . At the n -th step, the stationary condition is used to update the current parameter estimate \mathbf{x}_n as

$$\begin{aligned} \mathbf{x}_{n+1} = & \mathbf{x}_n + \left[\mathbf{A}_n^T \mathbf{W}_n \mathbf{A}_n + \sum_{i=1}^k \lambda_i \Lambda_i \right]^{-1} \\ & \left[\mathbf{A}_n^T \mathbf{W}_n (\mathbf{d} - \mathbf{a}(\mathbf{x}_n)) - \sum_{i=1}^k \lambda_i \Lambda_i \mathbf{x}_n \right], \end{aligned} \quad (13)$$

where \mathbf{W}_n and \mathbf{A}_n are the Huber weight matrix and the Jacobian of $\mathbf{a}(\mathbf{x})$ at \mathbf{x}_n , respectively. Two iterations were taken in this study and the starting model was CM3 or zero for new parameters.

4.2. Error Estimates

It remains to assign the standard deviations σ_k in eq. 11 under the assumption of uncorrelated errors. For the OHMs, the errors were simply assumed to be uncorrelated and were assigned according to the *a posteriori* residuals from CM3. Thus, for stations poleward of $\pm 50^\circ$ dipole latitude, $\sigma_X = \sigma_Y = 16$ nT and $\sigma_Z = 19$ nT, and for stations equatorward, $\sigma_X = \sigma_Y = \sigma_Z = 9$ nT. For satellite scalar data, $\sigma_F = 4$ nT was used. However, for satellite vector data,

the errors in measured X, Y, and Z are correlated due to attitude inaccuracies.

Olsen (2002) employs the correlated covariance matrix of Holme & Bloxham (1996) to account for the anisotropy in the attitude accuracy of the Ørsted vector data. It can be shown that the principle components of such a matrix lie in the directions of \mathbf{B} , $\hat{\mathbf{n}} \times \mathbf{B}$, and $\mathbf{B} \times (\hat{\mathbf{n}} \times \mathbf{B})$, with associated coordinate system denoted as (B, B_\perp, B_3) , where $\hat{\mathbf{n}}$ is the unit vector in the direction of the bore-sight of the star imager and \mathbf{B} is the observed magnetic field vector. The principle variances are then $(\sigma_B^2, \sigma_\perp^2, \sigma_3^2)$, where $\sigma_\perp^2 = \sigma_B^2 + |\hat{\mathbf{n}} \times \mathbf{B}|^2 \chi^2 + (\hat{\mathbf{n}} \cdot \mathbf{B})^2 \psi^2$ and $\sigma_3^2 = \sigma_B^2 + B^2 \psi^2$. ψ , χ , and σ_B are the standard deviations of the bore-sight direction, angle about the bore-sight, and scalar intensity, respectively. In this study, $\psi = 10$ arcsec, $\chi = 60$ arcsec before and 40 arcsec after 22 Jan, 2000 reflecting improvements in attitude accuracy, and $\sigma_B = 4$ nT consistent with σ_F . For IRLS, the residual vector in the (B, B_\perp, B_3) system and the principle standard deviations are used in eq. 11 and the resulting weight submatrix is rotated back into the (X,Y,Z) system.

The same basic scheme is used for Magsat vector data, except that any anisotropic treatment is precluded by lack of directional information from the attitude determination instruments. Therefore, the best that can be done is an isotropic treatment, i.e., let $\psi = \chi$. Attitude errors for Magsat are thought to be about 20 arcsec (Langel et al., 1981) and so let $\psi = 20$ arcsec. This leads to $\sigma_\perp^2 = \sigma_3^2 = \sigma_B^2 + B^2 \psi^2$ such that the principle variances are of the form $(\sigma_B^2, \sigma_\perp^2, \sigma_\perp^2)$. The principle direction of the first component is still \mathbf{B} , but the last two components exist in a linear subspace perpendicular to \mathbf{B} . Let the residual vector δB be decomposed into components δB_B and δB_3 along and in the plane perpendicular to \mathbf{B} , respectively. For IRLS, choose $\hat{\mathbf{n}}$ to be the unit vector in the direction corresponding to δB_3 , and so $\delta B = (\delta B_B, 0, \delta B_3)$ in the (B, B_\perp, B_3) system. From eq. 11, the B_\perp component will always be weighted as Gaussian, but the B_3 may not depending upon the value of $|\delta B_3|$. Thus, IRLS may impart some anisotropy in the plane perpendicular to \mathbf{B} .

4.3. Regularization and *A Priori* Information

In addition to magnetic field observations, information has been introduced either to restrict the set of admissible parameter estimates due to insufficient data (regularization) or to impart some physical knowledge to the problem that is otherwise not supplied by data or theory. As stated earlier, this information is in the form of ℓ_2 type norms on \mathbf{x} , and with the exception of *F*-region currents, is the same as in CM3. Main field SV is smoothed by two norms: 1) the mean-square magnitude of \vec{B}_r over the core-mantle boundary (CMB) over the span of the model, denoted as $\mathcal{Q}_{|\vec{B}_r|}$, and 2) the mean-square magnitude of the surface Laplacian of \vec{B}_r over the

Table 2. Damping parameter values.

Norm	Damping parameter (λ)	
$\mathcal{Q}_{ \ddot{B}_r }$	6.2×10^0	$(\text{nT}/\text{y}^2)^{-2}$
$\mathcal{Q}_{ \nabla_s^2 \dot{B}_r }$	6.2×10^{-8}	$(\text{nT}/\text{y}/\text{km}^2)^{-2}$
$\mathcal{Q}_{\ \mathbf{J}_{\text{eq}}\ }$	8.4×10^2	$(\text{A}/\text{km})^{-2}$
$\mathcal{Q}_{\ \nabla_s^2 \mathbf{J}_{\text{eq}, p>0}\ }$	3.8×10^{-2}	$(\text{A}/\text{km}^3)^{-2}$
$\mathcal{Q}_{\ \Delta \mathbf{B}_{\text{itd}}\ }$	6.3×10^4	$(\text{nT})^{-2}$
$\mathcal{Q}_{ \nabla_h^2 J_r }$ dawn	1.3×10^{-15}	$(\text{nA}/\text{m}^4)^{-2}$
$\mathcal{Q}_{ \nabla_h^2 J_r }$ dusk	1.3×10^{-15}	$(\text{nA}/\text{m}^4)^{-2}$
$\mathcal{Q}_{ \nabla_h^2 J_r }$ Ørsted	1.3×10^{-16}	$(\text{nA}/\text{m}^4)^{-2}$
$\mathcal{Q}_{\ \nabla_h^2 \mathbf{J}_h\ }$ dawn	1.3×10^{-2}	$(\text{nA}/\text{m}^4)^{-2}$
$\mathcal{Q}_{\ \nabla_h^2 \mathbf{J}_h\ }$ dusk	1.3×10^{-2}	$(\text{nA}/\text{m}^4)^{-2}$
$\mathcal{Q}_{\ \nabla_h^2 \mathbf{J}_h\ }$ Ørsted	1.3×10^{-2}	$(\text{nA}/\text{m}^4)^{-2}$
$\mathcal{Q}_{ J_r }$	4.2×10^{-2}	$(\text{nA}/\text{m}^2)^{-2}$

CMB and over the span of the model, denoted as $\mathcal{Q}_{|\nabla_h^2 \dot{B}_r|}$. Nightside ionospheric E -region currents are minimized by a norm, denoted as $\mathcal{Q}_{\|\mathbf{J}_{\text{eq}}\|}$, which measures the mean-square magnitude of the E -region equivalent currents, \mathbf{J}_{eq} , flowing at 110 km altitude over the nighttime sector through the year. In addition, these currents are further smoothed by a norm, denoted as $\mathcal{Q}_{\|\nabla_s^2 \mathbf{J}_{\text{eq}, p>0}\|}$, which measures the mean-square magnitude of the surface Laplacian of the diurnally varying portion of \mathbf{J}_{eq} at mid-latitudes at all local times. In the magnetosphere, the mean-squared magnitude of deviations from a dipole field in magnetic local time is damped at Magsat altitude (450 km), independent of D_{st} .

For CM3, the mean-square magnitude of the radial F -region currents were minimized at Magsat altitude at dawn and dusk. For CM4, the mean-square magnitude of the surface Laplacian of poloidal J_r (denoted $\mathcal{Q}_{|\nabla_h^2 J_r|}$) and \mathbf{J}_h (denoted $\mathcal{Q}_{\|\nabla_h^2 \mathbf{J}_h\|}$) were damped separately and on spheres at 430 km and 415 km for Magsat dawn and dusk, respectively, and at 750 km for Ørsted at all local times. In addition, because Ørsted samples continuous diurnal variations, the mean-square magnitude of J_r was damped over the same nighttime sector used in $\mathcal{Q}_{\|\mathbf{J}_{\text{eq}}\|}$ in order to stabilize meridional coupling currents associated with the EEJ and to allow inter-hemispheric coupling currents to still flow via \mathbf{J}_h . It is denoted as $\mathcal{Q}_{|J_r|}$. The values used for the damping parameters associated with these norms are listed in Table 2.

5. RESULTS AND DISCUSSION

5.1. Residuals

The unweighted residual mean and rms with respect to CM4 are given in 3, along with measurement counts, N . Residuals are provided according to two classifications: 1) poleward (“Polar”) and equatorward (“non-Polar”) of $\pm 50^\circ$ dipole latitude, and 2) local time from 0600 to 1800 (“Day”) or from 1800 to 0600 (“Night”). Magsat dawn and dusk are listed un-

der “Night” and “Day”, respectively. The (X, Y, Z) components are oriented (north, east, down), and the (B_B, B_\perp, B_3) components are described in Section 4.2 for the particular satellite. Fits to the OHMs are commensurate with those of CM3, as are the fits to the POGO and Magsat data. However, there does appear to be a redistribution in size of the rms values of the Magsat components: in particular, Y appears to be larger, but $F + B_B$ appears to be smaller. This, however, is consistent with attitude error considerations, which place a higher weight on the measurement magnitude at the expense of information in the perpendicular directions, and Magsat was in near-polar orbit in a strongly dipolar field. In addition, Magsat vector data is fit very poorly at high latitudes in components perpendicular to the ambient field; clearly unmodelled signal from polar field-aligned currents.

A comparison of Ørsted and CHAMP fits cannot be made with CM3. However, Olsen (2002) has derived a model based upon nightside Ørsted scalar data at all latitudes and vector data poleward of $\pm 50^\circ$ dipole latitude. The resulting rms values are 2.89 nT, 6.40 nT, and 3.25 nT for the $F + B$, B_\perp , and B_3 components, respectively, which is quite close to the non-polar, nightside values for CM4. In fact, Olsen (2002) may have been more stringent in the tolerance of outliers than in this study. As with Magsat, the vector data is fit poorly in horizontal components at high latitudes. Although CHAMP data was not fit by Olsen (2002), residual rms values with respect to that model were quoted to be 3.4 nT for non-polar and 5.4 nT for polar F . The CM4 non-polar, nightside rms certainly agrees well here, but the polar rms value is very high; almost 2.2 nT higher than that of Ørsted. In order to get a better picture of the nature of these residuals, samplings (every fifth point) were plotted in Fig. 3 in the (B_B, B_\perp, B_3) system for Ørsted, along with CHAMP F , versus both dipole latitude and universal time (UT) rendered in modified Julian days (MJD). Clearly, there is much dispersion at high latitudes in all components of both satellites. One can also see a general thickening of the δB_\perp residual band over the others at low latitudes, which is expected. δB_3 shows the existence of some possible systematic outliers which should be removed. As for behavior in UT, no major differences are seen before or after 1 January 2001 (denoted by the vertical dotted line), the dividing point before (after) which the final (provisional) D_{st} index was used, although δB_\perp and δB_3 may be slightly more dispersed after this date.

Because one of the strengths of the CM approach is the ability to properly divide the signal amongst the field sources, it is interesting to look at a residual progression, especially one that highlights the new capability of modelling Ørsted F -region fields. Thus, a progression was generated for the Y component of an Ørsted descending pass on 20 August 2001 beginning at 0700 UT and crossing the equator at 1230 MLT versus geographic latitude in Fig. 4. For a given panel, the symbols represent residuals with respect to the main field (up to degree 13) plus all

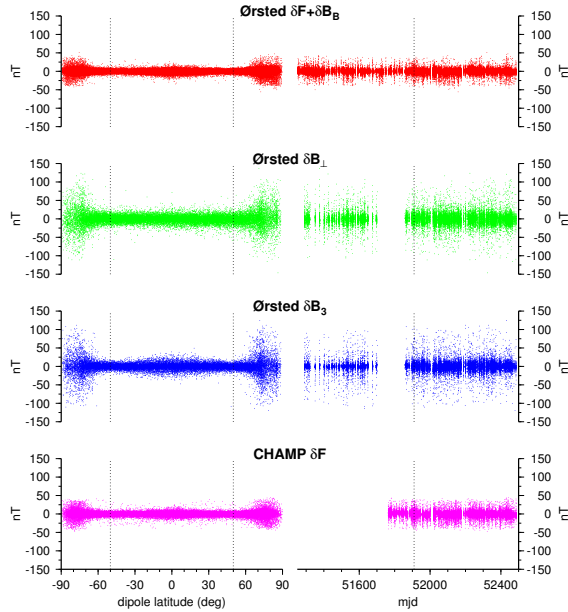


Figure 3. A sampling of the residual distributions for Ørsted and CHAMP as a function of dipole latitude (left) and universal time (right) rendered as modified Julian days (MJD). Every fifth point is plotted here. Vertical dotted lines in the left panel denote $\pm 50^\circ$ dipole latitude and in the right denotes 1 January 2001, which divides the earlier (later) days in which the final (provisional) D_{st} index was used.

fields labeled in the panels above; the red line is the prediction from the field labeled in the current panel. Clearly, the toroidal Y prediction from the F -region coupling currents is describing very well most of the variance in ΔY after removal of the main field. Indeed, Ørsted is able to detect the field due to the meridional current system associated with the EEJ, first reported to be seen in Magsat data by Maeda et al. (1982). Interestingly, a typical Magsat Y signature would be asymmetric with respect to the dip equator along a polar pass, with a crest (trough) to the south (north) of the dip equator. This is because the meridional currents upwell at the dip equator and then downwell within 10° to 20° on either side of it. Thus, eastward (westward) magnetic field is produced south (north) of the dip equator. The vertical dotted line in Fig. 4 shows the location of the dip equator and reveals that toroidal Y is closer to being symmetric with respect to the dip equator. This indicates that there is little vertical current flow directly at the dip equator and may suggest a shifting of meridional currents associated with the EEJ at this altitude. These currents and their implications will be discussed more in a later section.

5.2. Lithospheric Fields

Besides the obvious extension of main field SV to mid-2002, the lithospheric field (here taken to be the internal SH expansion corresponding to $n \geq 15$) is

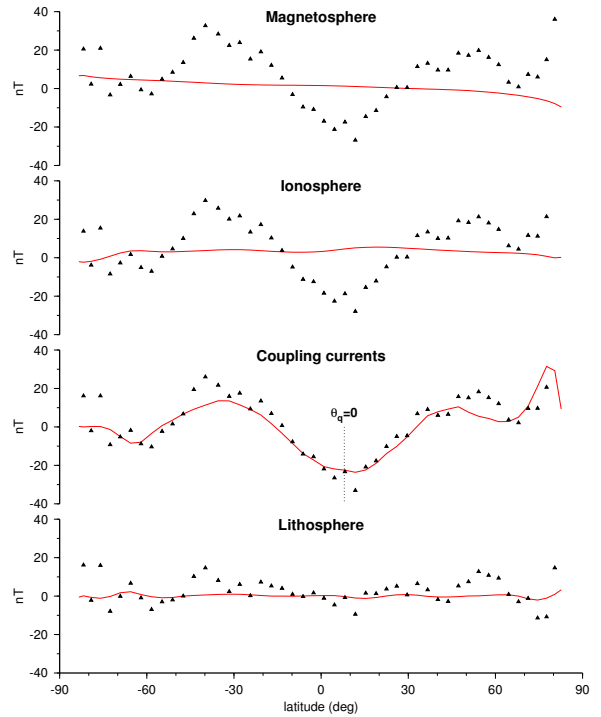


Figure 4. Residual progression for the Y component of an Ørsted descending pass on 20 August 2001 beginning at 0700 UT and crossing the equator at 1230 MLT versus geographic latitude. For a given panel, the symbols represent residuals with respect to the main field (up to degree 13) plus all fields labeled in the panels above; the red line is the prediction from the field labeled in the current panel. The vertical dotted line indicates the geographic latitude where the pass crosses the dip equator (about 8°).

one of two constituent fields that have changed the most over their CM3 counterparts, and the CM4 version is considered far superior. Its B_r component is shown in Fig. 5 at 400 km altitude, along with some of the more major tectonic lineations. The CM4 map has much fewer spurious, small-scale oscillations at low and mid latitudes, especially along the dip equator. This is shown perhaps more convincingly by a comparison of the Lowes-Mauersberger, R_n , spectra at Earth's surface in Fig. 6. R_n is the mean-square magnitude of the magnetic field over a sphere produced by harmonics of degree n , and at $n = 65$ the CM4 value is almost 5 times less than that of CM3. The departure begins arguably around $n = 25$ after which the CM4 spectrum falls increasingly below that of CM3, thus the difference is greatest where noise contamination would be the largest. The reasons for this may be multifold: 1) there is much denser coverage of satellite data in CM4, whereas the coverage in CM3 is known to exhibit several “holes”, 2) the proper treatment of attitude errors in Magsat may damp perpendicular errors, especially around the dip equator; and 3) t_{mut} is now computed more accurately, where before it could deviate from the true value by as much as 20 m and perhaps generate a distribution of spurious biases into the maps.

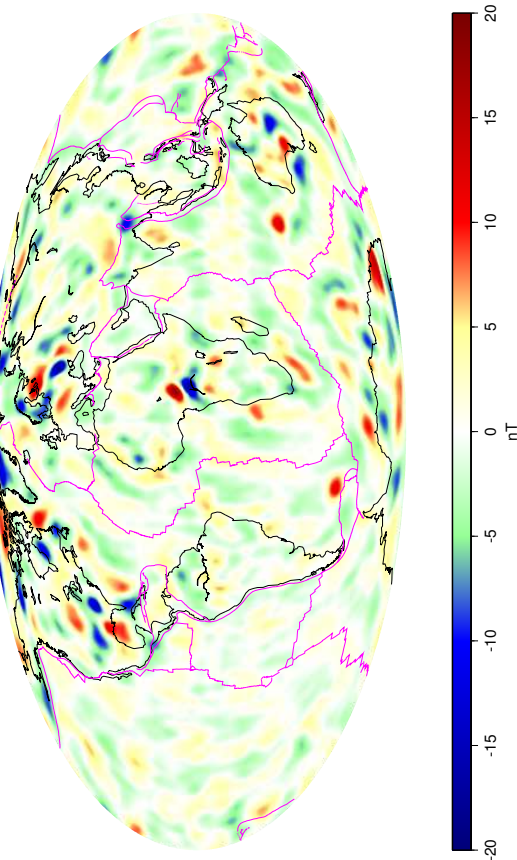


Figure 5. B_r component of the lithospheric field ($n = 15 - 65$) at 400 km altitude predicted by CM4 (Mollweide projection). Major tectonic lineations are drawn in magenta.

Focusing again on Fig. 5, several features align well with tectonic lineations such as the Aleutian trench, the Izu-Bonin trench, the Himalayan plateau, the mid-Atlantic ridge, and the Andes subduction zone. Several of these features strike north-south, an orientation that has been difficult to model in the past due to the use of north-south filters.

5.3. F -region Currents

Perhaps the largest difference between CM3 and CM4 is the resolution of toroidal fields generated by insitu F -region currents in the satellite sampling shells. Fig. 7 shows global maps of the J_r and J_{θ_q} components of these fields from CM4 within these shells. The top two panels are for fixed dawn and dusk MLTs on 21 March 1980 at 430 km and 415 km altitudes, respectively (mean altitudes for the Magsat data used in CM4). J_r shows the well known meridional currents associated with the EEJ upwelling along the dip equator and downwelling along side lobes at dusk, but no such feature at dawn. J_{θ_q} is much more intense than J_r and low QD latitudes and shows a clear reversal in flow direction between dawn and dusk. In addition, there is asym-

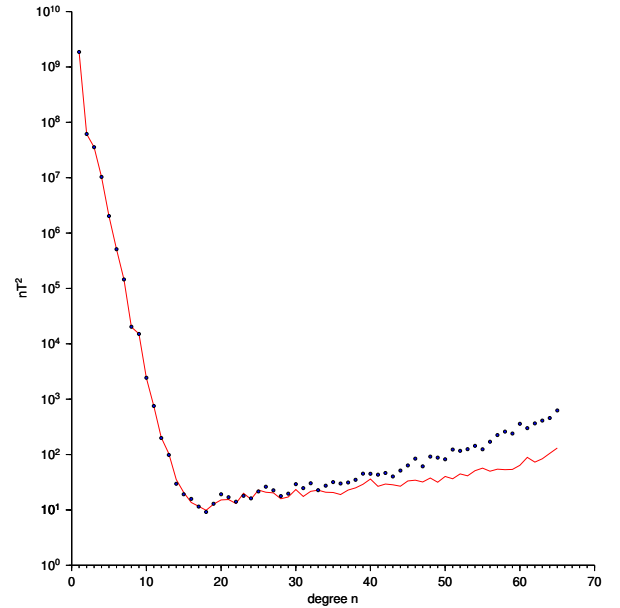


Figure 6. Comparison of the Lowes-Mauersberger (R_n) spectra for CM4 (red line) and CM3 (symbols) at Earth's surface. R_n is the mean-square magnitude of the magnetic field over a sphere produced by harmonics of degree n .

metric flow across the dip equator: a net flow to the north (south) during dawn (dusk). Although Olsen (1997a) investigated such currents during northern winter from Magsat data, similar behavior was observed and was attributed to inter-hemispheric connecting currents, which flow in opposite directions in the morning and evening. Furthermore, intensity differences are explained by the horizontal component of a solenoidal \mathbf{J} flowing in a restricted horizontal layer and compensating the radial component, which flows through a much wider vertical layer.

The bottom two panels are for fixed noon MLT and MUT on 21 March 2000 at 750 km (typical Ørsted altitude). There is indeed a band of strong upwelling in the Australian sector for fixed noon MLT that is offset to the south of the dip equator (the dip equator has been generated from the CM4 main field). Over S. America it appears to be weaker and a strong region of downwelling now dominates. The plausibility of this offset is supported, at least in the Indian sector, by the toroidal Y component predicted along the pass which crossed the dip equator at about $\phi = 79^\circ$ in Fig. 4. Although it occurred during northern summer, this component would be produced by just such a pattern in J_r . For fixed noon MUT, there is little if any banded structure in low latitude J_r outside of a few tens of degrees of local noon, which would be expected of a meridional current system that is associated with the EEJ.

As for J_{θ_q} , the fixed noon MUT map exposes a weakness in the present parameterization: there is no variation along lines of constant θ_q with t_{mlt} as would be expected from the oppositely flowing inter-

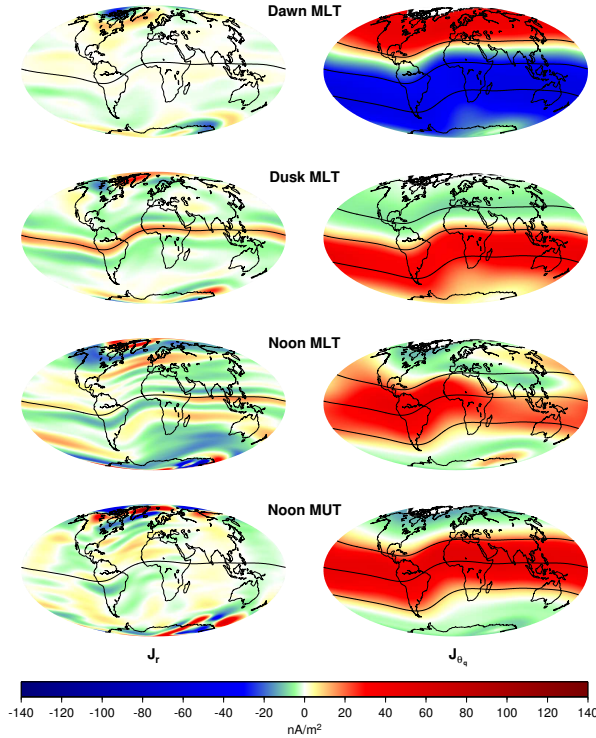


Figure 7. J_r (left) and J_{θ_q} (right) components of the F -region current density. From the top, the component pairs are for dawn MLT at 430 km, dusk MLT at 415 km, noon MLT at 750 km, and noon MUT at 750 km (Mollweide projections). The dip equator is plotted on all maps and the $\theta_q = \pm 60^\circ$ curves are plotted on the J_{θ_q} maps as well.

hemispheric currents detected by Magast at morning and evening (top two panels). However, there is variation in the map for fixed noon MLT. To see this, the $\theta_q = \pm 60^\circ$ lines have been plotted on the J_{θ_q} maps along with the dip equator. To see why this is so, recall from eq. 7 that J_{θ_q} is the component in the direction of $\nabla_h \theta_q$. Assuming $\|\nabla_h \theta_q\|$ is constant along lines of constant θ_q , then only $\partial f / \partial \theta_q$ changes along these lines. For a fixed season, this change comes from multipliers of the form $\exp(ip\phi_p(t_{\text{mut}}(t)))$. Thus, J_{θ_q} is constant along lines of constant θ_q when: 1) t , and therefore $t_{\text{mut}}(t)$, is constant, as in the fixed noon MUT map; or 2) $p = 0$, as in the fixed dawn and dusk MLT maps. Only fixed MLT maps produced by terms involving $p \neq 0$ will show variation along lines of constant θ_q since $t_{\text{mut}}(\phi_{d,o}) = t_{\text{mlt}} - \phi_{d,o}/15$ varies across the map.

5.4. Future Work

As for internal fields, the admission of SV models which are consistent with core dynamics, or at least the kinematics, should become a priority. Also, incorporation of low altitude CHAMP vector data will provide much useful information about the high degree lithosphere, and this will be an objective of fu-

ture CMs. The treatment of induced fields would be enhanced by using coupling matrices which describe lateral heterogeneities in the conductivity structure of the Earth.

As for external fields, inclusion of the full F -region current density vector will supply the degrees of freedom necessary to describe inter-hemispheric coupling currents in a continuous MLT sense. Clearly, another area for improvement is the treatment of polar current systems, which may entail some functionality based upon the interplanetary magnetic field or polar activity indices.

6. CONCLUSIONS

The POGO-Magsat based CM3 model has been extended and improved by the inclusion of Ørsted vector and scalar and CHAMP scalar data. In addition to the obvious extension of the main field SV model to mid-2002, this new model shows great improvement in the characterization of the lithospheric field manifested as a drastic decrease in high frequency noise content. The description of fields from F -region currents impinging satellite sampling shells has also been greatly enhanced by treating these currents as meridional, and in the case of Ørsted, treating them as diurnally continuous. Several of the items proposed for future study should be readily attainable in the near future. Lastly, the CM4 model and its forward code are available from the authors by request.

ACKNOWLEDGEMENTS

We would like to thank Mike Purucker for reselecting the Magsat vector data used in this study. We would also like to thank Peter Stauning and the other members of the OIST-4 organizing committee for allowing us the present our work in these proceedings.

REFERENCES

- Backus, G.E., 1986. Poloidal and toroidal fields in geomagnetic field modeling, *Rev. Geophys.*, **24**, 75-109.
- Constable, C.G., 1988. Parameter estimation in non-Gaussian noise, *Geophys. J.*, **94**, 131-142.
- Holme, R. & Bloxham, J., 1996. The treatment of attitude errors in satellite geomagnetic data, *Phys. Earth. Planet. Int.*, **98**, 221-233.
- Huber, P.J., 1964. Robust estimation of a location parameter, *Ann. Math. Statist.*, **35**, 73-101.
- Langel, R.A., Berbert, J., Jennings, T. & Horner, R., 1981. Magsat data processing: A report for investigators, *NASA Tech. Mem.*, **82160**, 1-178.

- Langel, R.A., Estes, R.H. & Mead, G.D., 1982. Some new methods in geomagnetic field modeling applied to the 1960-1980 epoch, *J. Geomag. Geoelec.*, **34**, 327-349.
- Langel, R.A., Sabaka, T.J., Baldwin, R.T. & Conrad, J.A., 1996. The near-Earth magnetic field from magnetospheric and quiet-day ionospheric sources and how it is modeled, *Phys. Earth. Planet. Int.*, **98**, 235-267.
- Maeda, H., Iyemori, T., Araki, T. & Kamei, T., 1982. New evidence of a meridional current system in the equatorial ionosphere, *Geophys. Res. Lett.*, **9**, 337-340.
- Olsen, N., 1993. The solar cycle variability of lunar and solar daily geomagnetic variations, *Ann. Geophys.*, **11**, 254-262.
- Olsen, N., 1997a. Ionospheric *F*-region currents at middle and low latitudes estimated from Magsat data, *J. Geophys. Res.*, **102**, 4563-4576.
- Olsen, N., 1998. The electrical conductivity of the mantle beneath Europe derived from C-Responses from 3 h to 720 h, *Geophys. J.*, **133**, 298-308.
- Olsen, N., 2002. A model of the geomagnetic field and its secular variation for epoch 2000 estimated from Ørsted data, *Geophys. J. Int.*, **149**, 454-462.
- Purucker, M.E., 2000. FTP mirror sites of Ørsted data, *Ørsted Newsletter # 6*.
- Richmond, A.D., 1995. Ionospheric electrodynamics using magnetic apex coordinates, *J. Geomag. Geoelec.*, **47**, 191-212.
- Sabaka, T.J., Langel, R.A., Baldwin, R.T. & Conrad, J.A., 1997. The geomagnetic field 1900-1995, including the large-scale field from magnetospheric sources, and the NASA candidate models for the 1995 revision of the IGRF, *J. Geomag. Geoelec.*, **49**, 157-206.
- Sabaka, T.J., Olsen, N. & Langel, R.A., 2002. A comprehensive model of the quiet-time, near-Earth magnetic field: phase 3, *Geophys. J. Int.*, **151**, 32-68.
- Walker, M.R. & Jackson, A., 2000. Robust modelling of the Earth's magnetic field, *Geophys. J. Int.*, **143**, 799-808.

Table 3. Unweighted residual statistics, where N is the number of data points and the mean and rms are in units of nT . “Polar” denotes data poleward of $\pm 50^\circ$ dipole latitude. “Day” denotes a local time from 0600 to 1800, otherwise “Night”.

Component		Polar			Non-polar					
					Day			Night		
		N	mean	rms	N	mean	rms	N	mean	rms
OHM_1AM	X	22,744	-0.50	17.58	—	—	—	19,826	0.05	10.49
	Y	22,766	0.09	14.37	—	—	—	19,796	0.10	7.37
	Z	22,771	0.03	22.76	—	—	—	20,300	-0.05	9.04
OHM_MUL	X	66,476	-0.07	16.91	28,517	-0.62	12.16	28,555	0.46	8.12
	Y	66,544	0.37	16.48	28,539	0.69	11.08	28,575	-0.54	6.24
	Z	66,390	-0.04	20.23	29,357	0.24	9.44	29,396	-0.14	6.56
POGO	F	11,857	0.05	4.68	8,789	-0.51	5.02	8,793	0.06	3.72
CHAMP	F	105,224	-0.33	9.23	70,439	-0.27	5.69	70,251	-0.07	3.68
Magsat Dawn	$F + B_B$	20,560	-0.31	5.49	—	—	—	23,368	0.06	3.00
	B_3	11,834	24.63	38.69	—	—	—	19,653	6.71	7.90
	X	11,834	0.18	24.53	—	—	—	19,653	0.20	4.61
	Y	11,834	-0.50	29.79	—	—	—	19,653	-0.26	5.83
	Z	11,834	-0.76	6.95	—	—	—	19,653	2.21	4.02
Magsat Dusk	$F + B_B$	19,127	0.12	6.35	19,404	0.02	3.90	—	—	—
	B_3	10,871	25.71	41.38	16,257	7.45	8.67	—	—	—
	X	10,871	-3.65	27.85	16,257	-0.45	5.36	—	—	—
	Y	10,871	1.55	30.59	16,257	-0.04	6.62	—	—	—
	Z	10,871	0.06	7.35	16,257	0.42	4.11	—	—	—
Ørsted	$F + B_B$	226,419	-0.15	7.04	169,631	-0.03	4.26	133,989	0.01	2.94
	B_\perp	54,077	-0.03	23.42	55,204	-0.72	10.58	19,241	-0.21	7.87
	B_3	54,077	-0.85	22.06	55,204	-0.14	8.87	19,241	-0.12	3.62
	X	54,077	0.10	21.74	55,204	0.07	7.46	19,241	-0.15	5.72
	Y	54,077	0.03	23.46	55,204	0.00	10.22	19,241	0.00	5.09
	Z	54,077	-0.01	7.48	55,204	0.36	6.96	19,241	-0.01	4.73